coatings

MDPI

Article

Extreme High-Speed Laser Material Deposition (EHLA) of AISI 4340 Steel

Tianci Li [1,2], Lele Zhang [1], Gregor Gilles Pierre Bultel [2,*], Thomas Schopphoven [2], Andres Gasser [2], Johannes Henrich Schleifenbaum [2,3] and Reinhart Poprawe [2]

1 School of Mechanical, Electronic and Control Engineering, Beijing Jiaotong University, Beijing 100044, China; tianci99.li@gmail.com (T.L.); llzhang1@bjtu.edu.cn (L.Z.)
2 Fraunhofer Institute for Laser Technology ILT, Steinbachstr. 15, 52074 Aachen, Germany; thomas.schopphoven@ilt.fraunhofer.de (T.S.); andres.gasser@ilt.fraunhofer.de (A.G.); johannes.henrich.schleifenbaum@ilt.fraunhofer.de (J.H.S.); reinhart.poprawe@ilt.fraunhofer.de (R.P.)
3 DAP-Digital Additive Production, RWTH Aachen University, Steinbachstr. 15, D-52074 Aachen, Germany
* Correspondence: gregor.bultel@ilt.fraunhofer.de

Received: 27 October 2019; Accepted: 19 November 2019; Published: 21 November 2019

Abstract: A variant of conventional laser material deposition (LMD), extreme high-speed laser material deposition (German acronym: EHLA) is characterized by elevated process speeds of up to 200 m/min, increased cooling rates, and a significantly reduced heat affected zone. This study focuses on the feasibility of using EHLA to apply material onto Fe-based substrate materials with AISI 4340 as a filler material. We studied how three different build-up strategies—consisting of one, three, and five consecutive deposited layers and hence, different thermal evolutions of the build-up volume—influence the metallurgical characteristics such as microstructure, porosity, hardness, and static mechanical properties. We propose a thermo-metallurgical scheme to help understand the effects of the build-up strategy and the thermal evolution on the microstructure and hardness. The tensile strength of the build-up volume was determined and is higher than the ones of forged AISI 4340 material.

Keywords: EHLA; hardness; AISI 4340; microstructure; build-up strategy; repair

1. Introduction

AISI 4340 is a low alloyed structural steel which is widely used in the industry for its properties such as high strength and toughness [1]. It is used for connecting links of helicopter and rotor hubs for its exceptional fatigue strength [2], for machine parts because of its advantageous combination of ductility, toughness and strength [3], and in nuclear power plant components [4]. If these high-quality components out of the AISI 4340 material fail, repair with effective procedures is an important means of reducing costs and extending service life.

Much research has been done to investigate the feasibility of repairing such structures and various test methods have been used to evaluate them. One of the most frequently used repair technologies is the galvanic deposition of hard chromium coatings which have a high resistance to wear and corrosion. However, the high tensile stresses introduced by hard chrome in the layer-substrate interface reduce the life cycle fatigue. Voorwald et al. [5] applied chromium layers to AISI 4340 steel and the results showed that the bending fatigue strength for rotating specimens was reduced to 61% and 65% for 10^5 and 10^7 cycles, respectively, compared to the blank steel. Moreover, the hard chromium process uses hexavalent chromium, which is harmful to the human health and the environment. Bonora et al. [6] investigated a thermal spraying technology (HVOF: High-velocity-oxygen-fuel) to coat the AISI 4340 material for aeronautic applications. The results showed cracks in the layers as well as in the transition between

layer and substrate. The applied powder particles bond to the substrate by mechanical clamping, which leads to tensile residual stresses and reduces the fatigue life of the deposited layers. Wu et al. [7] studied the feasibility of repairing AISI 4340 components through friction stir processing (FSP). In this study filling blocks were used as filling material. The filler blocks were first fixed to the substrate by electron beam welding, then the filler blocks were joined to the material to be repaired using a friction stirrer. The results showed no defects in the repaired zone. The measured maximum tensile strength was 91.8% compared to that of a forged structure and a ductile-brittle fracture was observed.

LMD has also widely been used to repair parts made of this low-alloy steel. LMD can be used to repair and functionalize surfaces thanks to its advantages, such as the metallurgical bonding between the deposited layer and the substrate [8], the defined and well controlled energy deposition [9], and the reduced heat affected zone (HAZ) [10]. Shi et al. [11] used laser cladding as a repair process for AISI 4340. They investigated the tensile strength of the samples after cladding. The specimens were prepared by adding a notch with the dimensions of 13.73 mm in length and 0.7 mm in thickness to the center of a plate-shaped substrate, and filling the notch with the AISI 4340 filler by LMD. Then, the excess cladded layer was removed by a CNC machine to generate a flat surface finish. The specimens were taken out from the plate and machined by wire cutting. Tensile test results indicated that the elongation of the specimen was 0.6%. An explanation for the brittleness was given by the detection of untempered martensite in the cladded area and the HAZ zone, which leads to high hardness and low ductility and toughness. Chew et al. [12] investigated the fatigue performance after cladding AISI 4340 on substrates out of the same material. The authors prepared the specimens by adding a pre-clad groove, filling the groove with AISI 4340 by LMD, and finally grinding them back to the original surface. Non-cladded 4340 steel substrate specimens with the same geometry as the cladded ones were prepared as a reference. The results showed that the thickness of the heat affected zone was approximately 620 µm. Hardness decreased from the cladded zone to the heat affected zone and substrate from 560 to 320 HV. The fatigue strength (S-N curve) of the substrate specimens is 685 and 475 MPa for the cladded specimen. Sun et al. [13] cladded AISI 4340 filler onto AISI 4140 substrates through LMD. Porosity and bonding defects between consecutive layers were detected. The measured porosity ratio was approximately 3.3%. The tensile strength was 1398 MPa and the elongation 1.7%, which indicates the brittleness of the cladded layers.

Low productivity and low-cost efficiency, however, limit using LMD in large-volume coating, repair, or additive manufacturing applications [14]. EHLA process is a new approach to overcome these shortcomings [15]. The EHLA-technology is characterized by elevated deposition speeds of 20 to 200 m/min, which is a factor of 10 to 100 compared to conventional LMD. Those welding speeds can be realized due to the special process management of the EHLA process that consists of a special control of the trajectory and velocity of powder particles through the laser beam with the goal to couple the energy of the laser beam primarily into the powder particles instead of into the substrate. The powder particles are thus melted while they are still above the substrate. Only a small portion of the laser power is transferred to the substrate to create a thin melt pool on the surface of the substrate. As a result, EHLA can achieve a narrow HAZ for a single layer in the range of 5 to 10 micrometers [14]. For this reason, it can deposit material onto heat-sensitive materials, i.e., crack sensitive materials which cannot be processed with the conventional LMD process [15,16].

However, ensuring that repaired parts meet the specified service requirements remains a scientific issue for laser material deposition processes [17] for it is essential that the mechanical properties of the base materials are not damaged. This study examines for the first time the use of the EHLA process using the filler material AISI 4340 for repair applications. Different build-up strategies and thus different interlayer temperatures are investigated for metallurgical quality, hardness, and microstructure. In addition, we propose a simplified thermo-metallurgical scheme for AISI 4340 based on the experimental results. This scheme visualizes the relationship between build-up strategy, temperature evolution, microstructure, and hardness of the cladding of AISI 4340 with the EHLA process. By better understanding how the build-up strategy influences the properties, one can develop

enhanced process parameters for repair applications using EHLA while taking the requirements towards mechanical properties into account.

2. Experimental Method

The investigation was conducted in four phases. First, we studied how the process parameters such as laser power, powder mass flow, volume of carrier gas, and the offset between two adjacent tracks influenced the deposited material. The aim of this phase was to obtain process parameters for a single layer with low porosity, metallurgic bonding between the substrate and the layer, and without any cracks. Second, the best process parameters were used for material build-up. Multiple layers were deposited in order to build up a total layer thickness of 3 mm. The total layer thickness of 3 mm was achieved using three different build-up strategies that were characterized by the deposition of one (strategy a), three (strategy b), and five (strategy c) consecutive layers as a set. After each set of deposited layers, there was a waiting time to cool the build-up volume to approximately 60 °C. The metallurgical quality, microstructure, and hardness corresponding to each build-up strategy was studied. In addition, we propose a simplified thermo-metallurgical scheme for AISI 4340 based on the experimental results. This scheme visualizes the relationship between build-up strategy, temperature evolution, microstructure, and hardness of the cladding of AISI 4340. Finally, a volume of 10 mm in thickness was built up with strategy c to test the tensile properties. The flow chart for the experimental approach is shown in Figure 1.

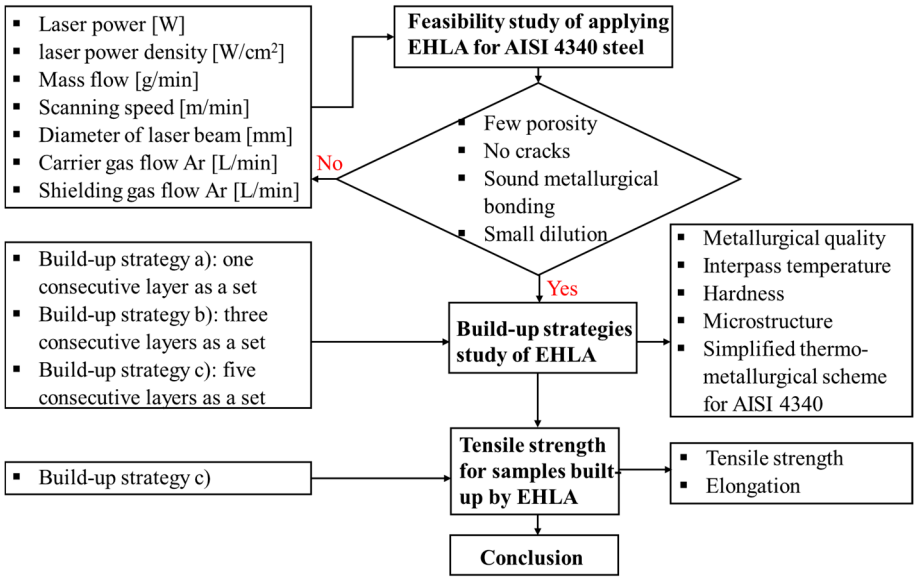

Figure 1. Flow chart of experimental development.

2.1. Experimental Process Development

Figure 2 shows a picture and a schematic representation of the EHLA process. The EHLA machine used consists of a spindle, a focusing optic, and a coaxial powder nozzle. A diode laser with a maximum laser power of 4000 W was used as a beam source, and a 600 µm diameter fiber for the connection to the system. The injection angle and the stand-off are parts of the parameters that are used to adjust the trajectory of powder particles through the laser beam and thus the distribution of the absorbed laser power into the powder gas jet and the substrate. In this paper, the powder particles are injected under an angle of approximately 20 degrees and the stand-off is about 10 mm. The operation was controlled by CNC. The powder is fed by a pneumatic twin powder feeder. We studied divergent parameter combinations for a single layer and investigated the microstructure (pores, cracks, bonding quality, thickness, etc.) of the cross-section of the deposition accordingly, and those results feeded back to the

process parameters. We chose the most suitable parameters for AISI 4340 from those experiments. The process parameters used are shown in Table 1.

All the three experiments were carried out with a meandering scan path, as shown in Figure 3. The overlap ratio between two tracks in the same layer was approximately 70%.

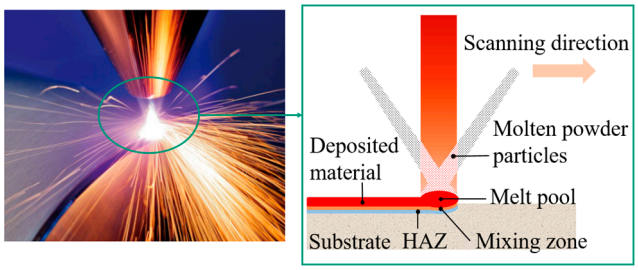

Figure 2. Picture of the EHLA process (coating of a rod) and scheme of the EHLA process.

Table 1. Process parameters used for the manufacturing of layers using EHLA.

Laser Power [W]	Scanning Speed [m/min]	Carrier Gas Flow Ar [L/min]	Offset between Two Adjacent Tracks [mm/360°]	Shielding Gas Flow Ar [L/min]	Powder Mass Flow [g/min]	Diameter of Laser Beam [mm]	Laser Power Density [W/cm^2]	Wave Length [nm]
2200	30	5.5	0.35	10	18.6	1.2	1.95×10^5	900–1100

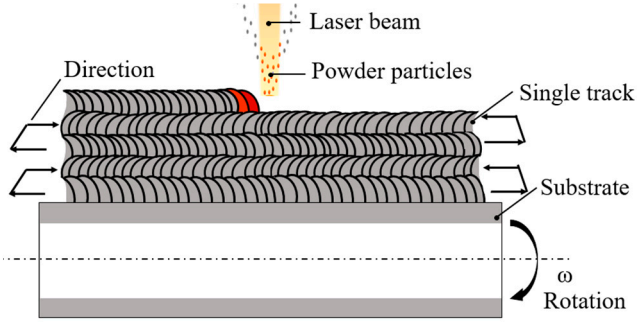

Figure 3. Scanning pattern to deposit multiple layers using EHLA.

2.2. Substrate and Filler Materials

Seamless steel tubes of low carbon steel E355 were used as substrate. The condition of the tubes is cold drawn (+C) with no final heat treatment. Longitudinal tensile tests at room temperature according to the DIN EN ISO 6892-1:2016 [18] were carried out by the supplier with specimen dimensions of 12.64 × 5.00 stating that the tensile strength (*Rm*) is 828 MPa and 12.0% elongation (A5). The hardness of E355 in this condition is approximately 270 HV. Dimensional inspection and visual examination were conducted according to the manufacturer's procedure. The outer diameter and inner diameter of the E355 steel tube were 50 and 40 mm, respectively. The chemical composition is shown in Table 2. The surface of the substrate was sandblasted and cleaned with alcohol before being processed with EHLA.

Table 2. Chemical composition of the E355 substrate material (in wt %).

Fe	C	Nb	Al	Si	Mn	S	P
Bal.	0.175	0.012	0.028	0.18	1.33	0.004	0.013

Low alloyed steel AISI 4340 powder was used as a filler material. The chemical composition of the powder is shown in Table 3. It is a gas-atomized spherical powder with 95% of the particle diameters in a range from 25 to 53 µm. Figure 4 shows SEM pictures of the 4340 powder at different magnifications.

Table 3. Chemical composition of the AISI 4340 powder (in wt %).

Fe	C	Cr	Ni	Mo	Si	Mn	S	P
Bal.	0.38–0.43	0.7–0.9	1.65–2.00	0.2–0.3	0.15–0.35	0.6–0.8	0.03	0.03

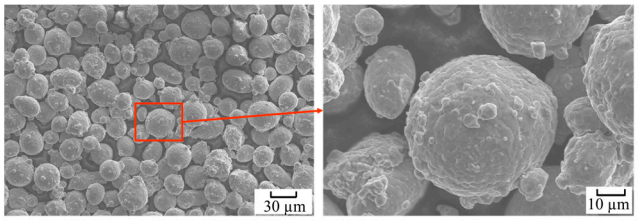

Figure 4. SEM micrographs of the 4340 powder at two different magnifications.

2.3. Metallurgical Quality Characterization

The cross-sections of the samples were polished and etched with 3% nital (97% ethanol and 3% nitric acid). Porosity, cracks, and metallurgical bonding between the layer and substrate were investigated by the use of optical microscope (OM) (Microscope Axio Imager Objective A-Plan Zeiss, Germany) for a single layer. Scanning electron microscope (SEM) (Leo1455EP, Zeiss, Germany) was used for the characterizing the morphology of different zones for a volume built up by different strategies.

2.4. Interpass Temperature Measurement of Volumes Built-Up by Three Strategies

The interpass temperature was measured by means of a contact thermometer (GOF 130, Fluke, Germany), shown in Figure 5. The temperature was measured on the surface of the last layer of each set immediately after it was completed. This was done for all three build-up strategies. The positions of measurements were at the beginning, middle, and ending side of the deposition surface and the highest temperature was recorded.

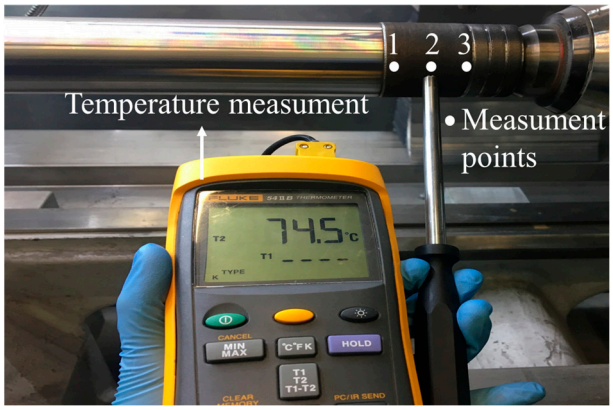

Figure 5. Measurement of the temperature of the last layer after each set of consecutive layers.

2.5. Hardness Measurement of Single Layer and Volumes Built-Up by Three Strategies

The nanoindentation test was employed to investigate the micro-hardness of a single layer. Additionally, the hardness of the layers, HAZ, and substrate of volumes built-up by three strategies was measured according to Vickers (HV 0.1). Three positions, from the left to the right side, were selected and three test lines were defined for each position. The horizontal distance between the lines was 50 µm and the distance between two measurement points was 25 µm, as shown in Figure 6. A total of 76 points were measured on a length of 3.8 mm, including the deposited layer, HAZ, and the unaffected substrate.

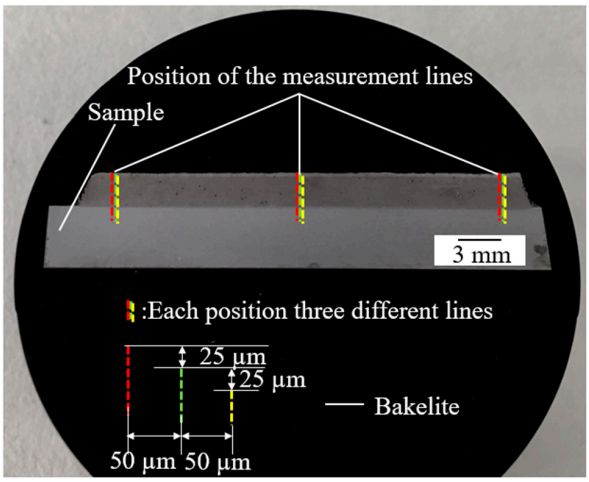

Figure 6. Arrangement of measurement points for Vickers hardness testing.

2.6. Tensile Test

Compared to the build-up strategy a and b, build-up strategy c has the highest productivity (build-up rate). This strategy also produced the lowest porosity. Therefore, build-up strategy c was utilized to obtain a sufficient volume (10 mm in thickness) for the manufacturing of tensile test samples. The tensile test was performed according to the DIN EN ISO 6892 standard [19], which specifies the tensile strength test method of metallic materials and defines the mechanical properties that can be determined at room temperature. The dimensions of the round tensile samples are specified in DIN 50125. The DIN 50125-B form was selected because this standard required the smallest dimension of testing samples. The manufacturing scheme and sample dimensions are shown in Figure 7.

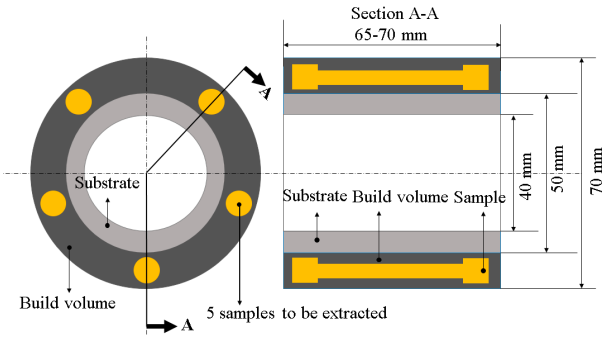

Figure 7. Tensile sample manufacturing scheme and geometry of the volume built up.

3. Experimental Results

3.1. Porosity

Figure 8 shows the cross-section of an EHLA layer deposited through the parameters shown in Table 2. Low porosity was observed in the layer. Lack of laser power density and defects in the powder particles are some of the reasons that cause porosity in the deposition. Heat dissipation into the cold substrate is one of the causes for the porosity between the base material and first layer. The EHLA parameters developed in this work minimize the possibility of porosity building in both the deposited layer and the interface.

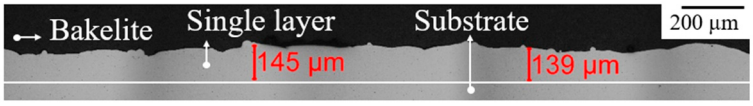

Figure 8. OM photograph of cross-section of a single layer.

3.2. Cracks

For the specimen deposited with the EHLA parameters shown in Table 2, observable-crack-free depositions were obtained, as can be seen in Figures 8 and 9. There are no cracks observed neither within the layer nor between the layer and substrate. It can be concluded that EHLA is applicable for the single layer deposition of AISI 4340.

3.3. Dilution and Bonding

Figure 9 shows a light microscope photograph of a cross-section of a single layer deposited using EHLA. The sample has been etched in order to highlight the HAZ. Metallurgical bonding without any defects and low dilution between the substrate and the deposited layer is achieved with the EHLA process. Compared to the conventional LMD, EHLA produces a minimum dilution of the cladding layers and results in a small HAZ. The thickness of the HAZ is approximately 50 µm. The relatively small HAZ is necessary to reduce deformation and stresses along with achieving high dimensional accuracy and integrity of the final products [20,21].

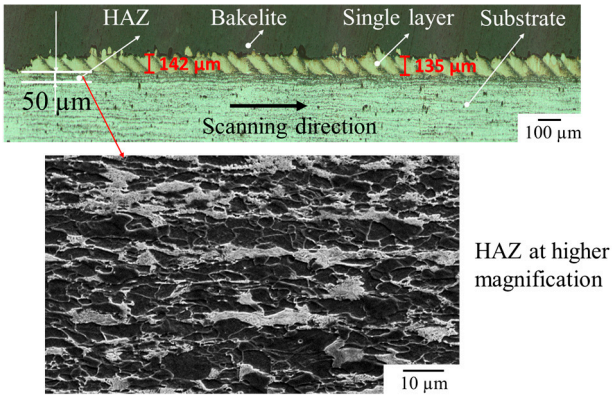

Figure 9. Photography of a cross-section of an etched single deposited layer and HAZ in higher magnification.

3.4. Microhardness

Figure 10 shows the hardness distribution within a single layer measured by the nanoindentation test. A single layer is created by overlapping individual tracks. The sample, also depicted in Figure 10, has been etched to highlight the individual tracks. As a track is deposited, the previous track is heated up and partly remelted, resulting in a change of the microstructure due to tempering effects. This effect is visualized by etching the sample. The results indicate that the hardness decreases in the overlap zone; the mean value of hardness in the overlap zone and non-overlap zone was 689 and 543 HV, respectively, it is approximately 100 HV lower than in the area of the track that has not been reheated and remelted. Figure 10 shows a cross-section of a single layer at higher magnification. It shows the microstructure in the HAZ and bonding zone, between two individual tracks and within one track. It also shows a metallurgical bonded layer without any defects between individual tracks. An inhomogeneous morphology can be seen in the layer's microstructure with a darker band between each track caused by the tempering. Tempered martensite broadly appears darker compared to the un-tempered martensite in an etched sample [22]. Martensite tempering due to laser heating for deposition of successive layers resulted in decomposition of martensite into ferrite and cementite [11]. Thus, the microhardness in the overlap zone of the specimen is lower compared to that of the hardness for non-overlap zone.

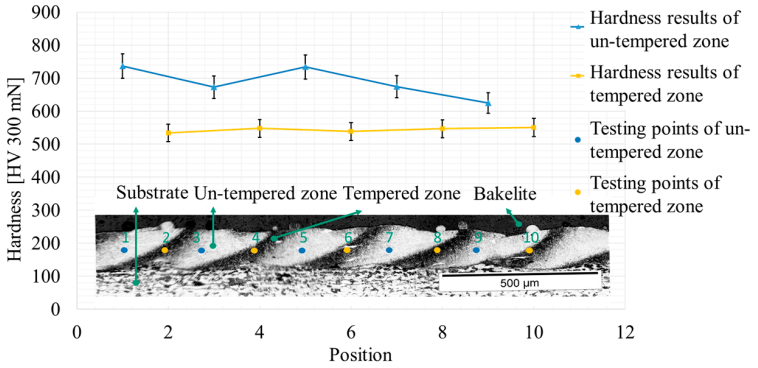

Figure 10. Hardness distribution within a single layer.

4. Build-Up Strategy Research of EHLA

4.1. Metallurgical Quality of Deposited Samples

4.1.1. Cracks

For all build-up strategies—a, b, and c—crack-free deposits were obtained (see Figure 11) in spite of the different maximum temperatures achieved. It can be concluded that all three process strategies can be applied for crack-free deposition of AISI 4340 onto E355 with the EHLA process.

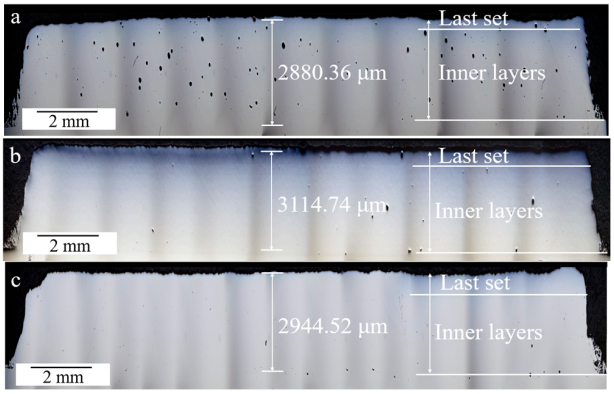

Figure 11. OM photographs of cross-sections built up by strategy (**a**) one single layer as a set; (**b**) three layers as a set; (**c**) five layers as a set.

4.1.2. Porosity

The porosity was measured by the optical microscope, and was calculated by the percentage of the whole area of pores in the cross section, shown in Figure 12. The deposition was cut into three parts in the length direction due to the limiting space in the block, and porosity were measured for all the three parts. As can be observed in Figure 11, build-up strategy a produces an increased amount of pores. The average value of porosity for build-up strategy a was found to be approximately 3.45% and for strategy b 0.22%. The average value of porosity for strategy c was the smallest with a value of 0.15%. Lack of fusion between two consecutive layers enhances the risk of pores forming during a multilayer deposition. Additionally, powder particles will remain un-melted on the surface of the previous layer as surface impurities and can contribute to pores forming on the subsequent deposited layer [23]. These defects are decreased when heat input increases. Another cause of porosity is the difference of speed for different powder particles. Powder particles at low velocity are incapable of penetrating into the liquid, or at high velocity are likely to drag in air cavities, which will be entrapped into the melt pool due to the limited time of that the melting pool is in a liquid state [24]. Continuous and higher heat input is sufficient to both get the particles melted and heat the previous deposited layer, which seems to minimize the possibility of porosity.

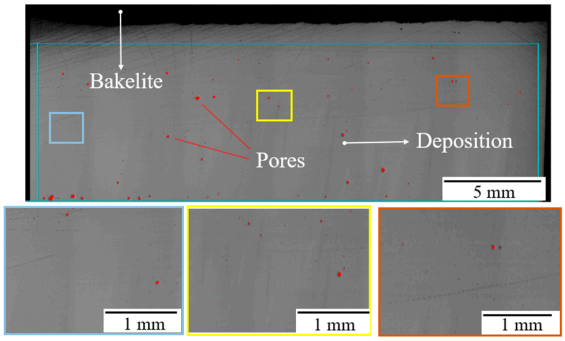

Figure 12. Cross section and porosity analysis of the 4340 deposition.

4.2. Interpass Temperature of Volumes Built-Up by Three Strategies

The highest temperature measured after depositing one layer (build-up strategy a was 160 °C and it took an average 5 min to fall down to 60 °C. The highest temperature measured for build-up strategy b (three consecutive layers) was 250 and 450 °C for strategy c (five consecutive layers), and the average cooling down time to 60 °C is 12 and 20 min, respectively, as shown in Figure 13.

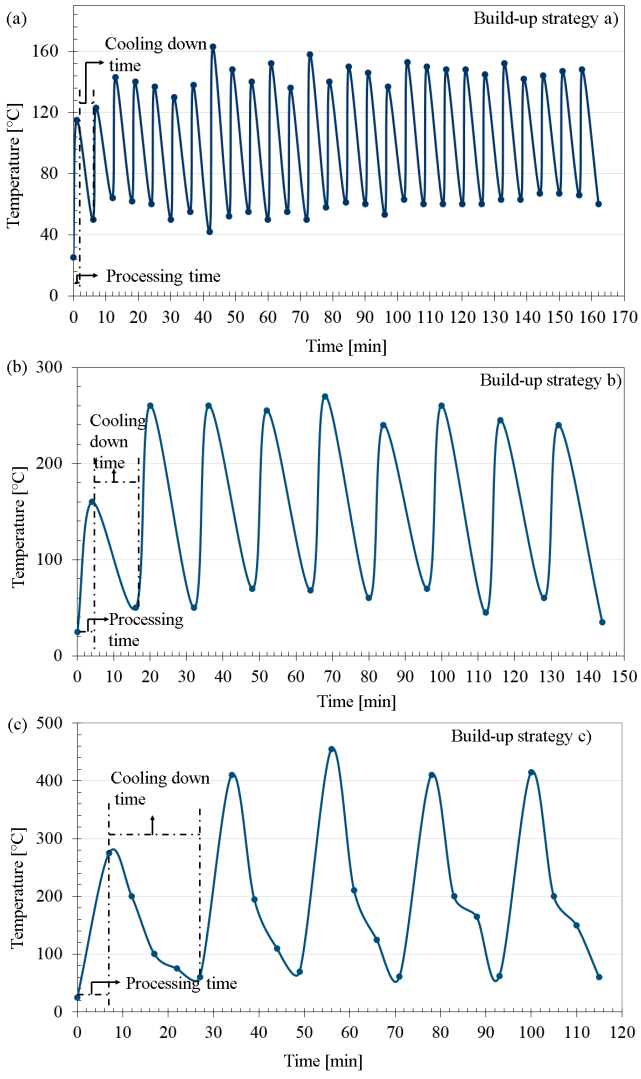

Figure 13. Surface temperature evolution for build-up strategy (**a**) one single layer; (**b**) three consecutive layers; (**c**) five consecutive layers as a set.

4.3. Hardness Distribution of Volumes Built-Up by Three Strategies

Figure 14 shows the perpendicular microhardness profile along the cross-section of the entire build-up, dilution zone, HAZ, and base material for different build-up strategies for one position, as can be seen in Figure 6. When hardness at different positions of a given sample is compared, the highest hardness value appears in the last set of layers with a value of 600, 550, and 300 HV 0.1 for strategy a, b, and c, respectively. Hardness decreases from the last set of layers to the inner layers. The average hardness of layers is 470 (standard deviation: 105 HV), 350 (standard deviation: 62 HV), and 260 (standard deviation: 38 HV) for strategy a, b, and c, respectively. There is a reduction of hardness in the HAZ for all the three build-up strategies, until the hardness reaches the level of the base material. The dimension of the HAZ zone is between 200 and 300 µm. The hardness experiences a sharp drop to the values in the HAZ, then it increases in the substrate for build-up strategies b and c. The drop of hardness is assumed to be a result of a complex time–temperature cycle introduced by different strategies. Regarding the deposition of a set of layers, there is an implicit heat treatment: By the deposition of one single layer onto a preceding layer; and by the warming up of the part during the deposition of a set of layers. Those different amounts of heat transfer to the substrate with the different holding time, resulting in different microstructures in the HAZ are shown in Figure 18, and the hardness is different accordingly.

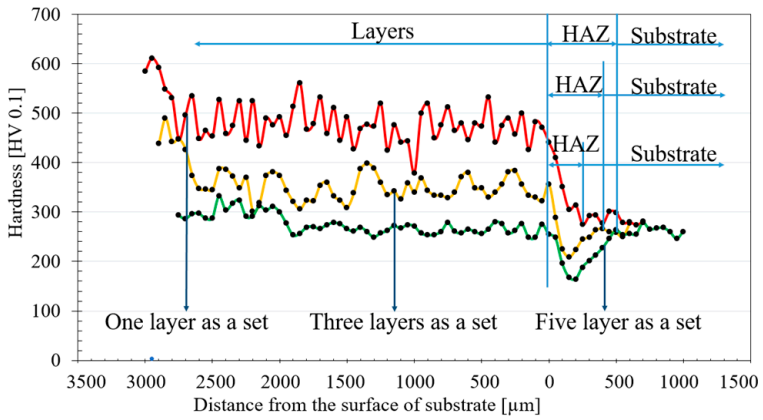

Figure 14. Hardness distribution in the volumes built with three different build-up strategies.

4.4. Microstructure of Volumes Built-Up by Three Strategies

The width of the HAZ is different for the three build-up strategies, which can be observed in Figures 15–17. The HAZ is defined by the changes of hardness from the cladded layer to the substrate. The width for strategy a is the smallest with a value of approximately 100 µm, and the hardness of the HAZ is higher than the hardness of the substrate. The HAZ is approximately 200 and 400 µm thick for b and strategy c, and the hardness drops from the deposited layers to the HAZ and then increases to the value of the substrate.

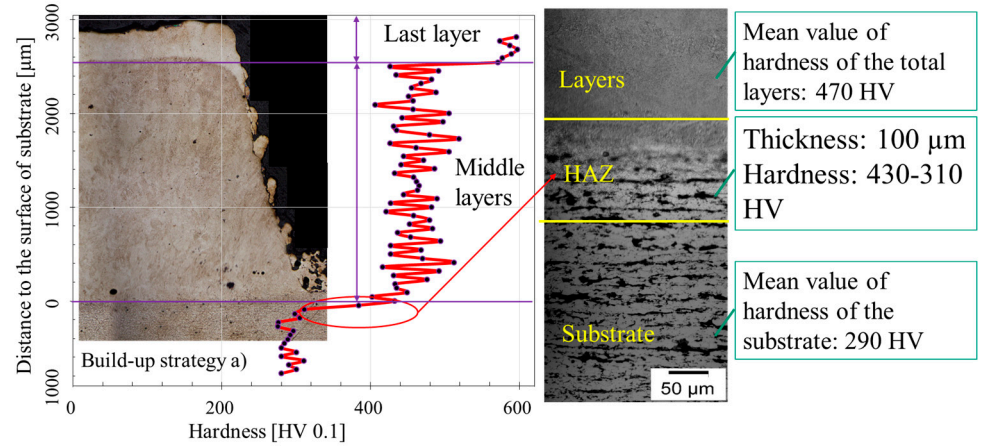

Figure 15. Hardness distribution and its corresponding light microscope photography for strategy a: One single layer as a set.

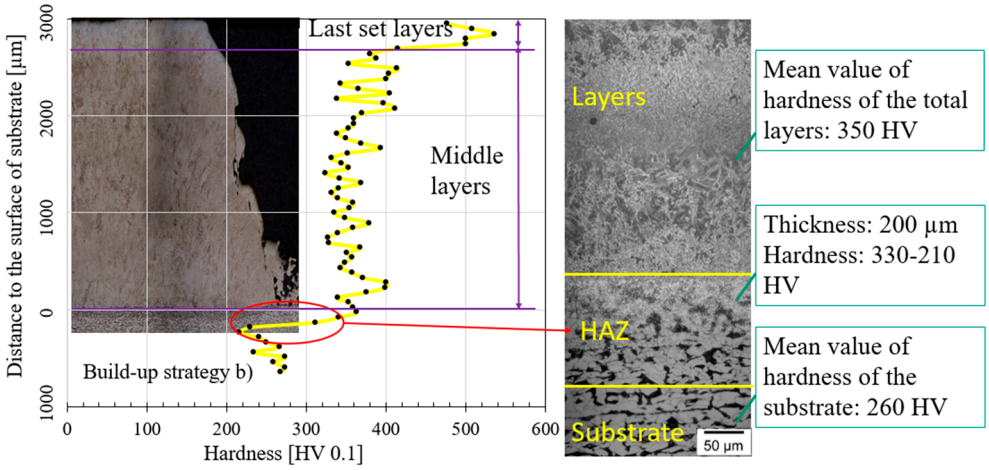

Figure 16. Hardness distribution and its corresponding light microscope photography for strategy b: Three layers as a set.

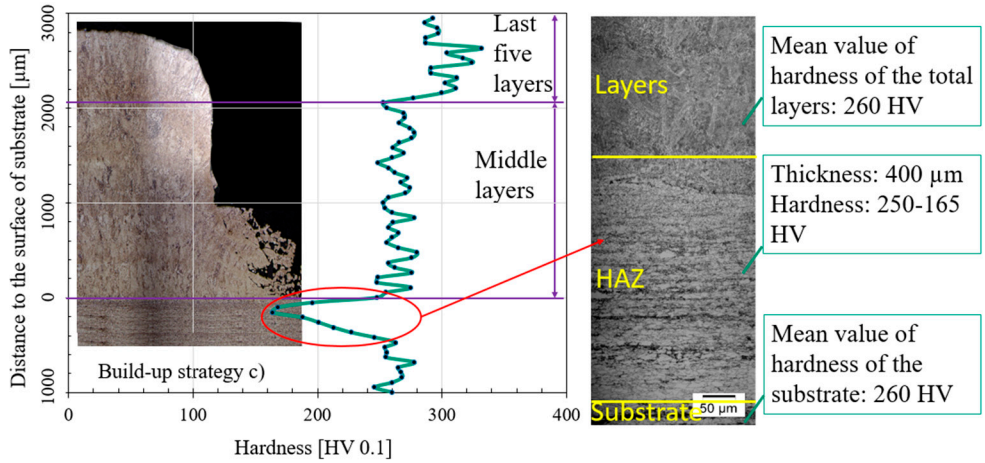

Figure 17. Hardness distribution and its corresponding light microscope photography for strategy c: Five layers as a set.

The microstructures of the last set of layers, the inner layers, the HAZ, and the substrate of the three different build-up strategies are illustrated in Figure 18. For the build-up strategy a, there is a cooling time between each layer, which allows martensite to form, as can be seen in Figure 18a. Figure 18b shows some needle-like martensite, tempered martensite, and ferrite. In the boundary

zone between the first layers and the substrate, the microstructure is finer than that in the inner layers, and a drop of hardness can also be seen (see Figure 15 for the build-up strategy b, the microstructure is coarser than that of strategy a. High temperature and longer holding time (strategy c), which is also shown in Figure 13, results in more ferrite forming and a coarser microstructure. For strategy c, the portion of ferrite increases and the portion of tempered martensite decreases. The deposition microstructure changes according to the build-up strategies, as the strategies have an effect on the process temperature and cooling rate.

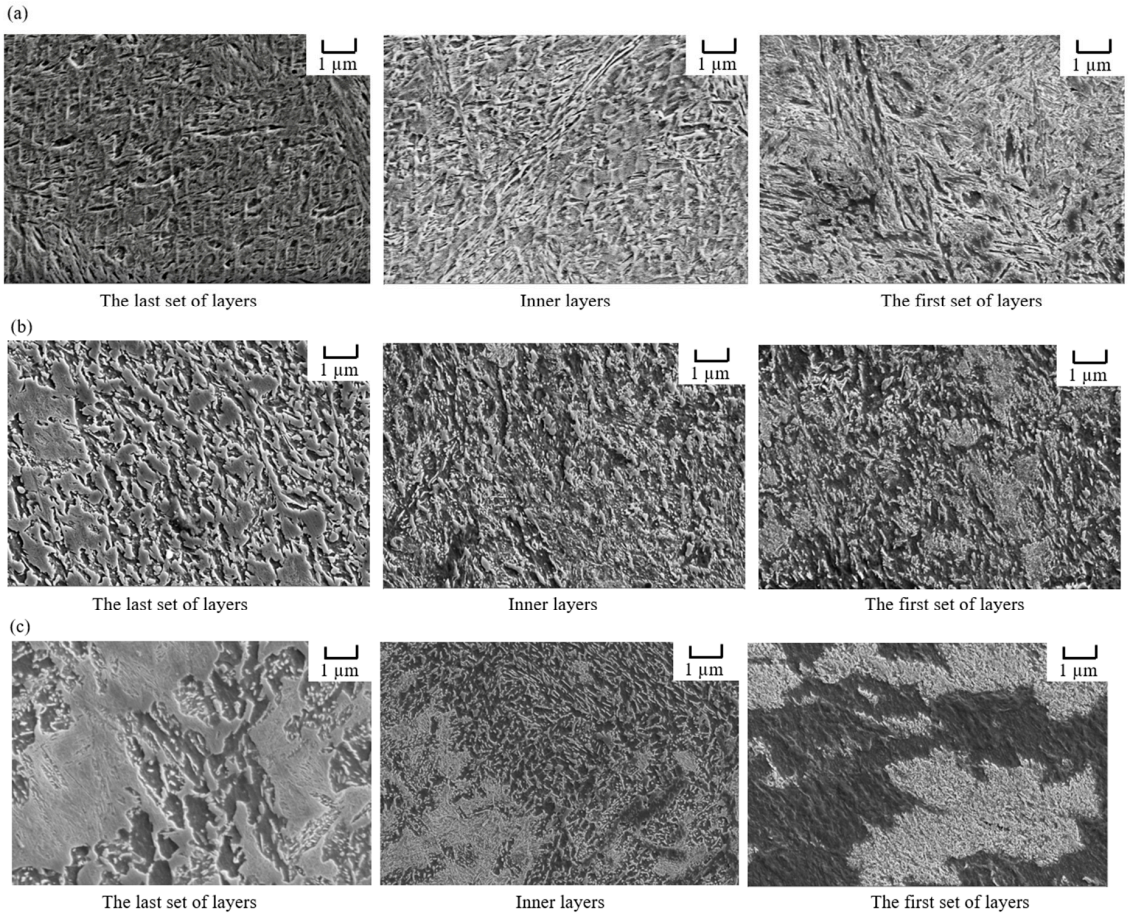

Figure 18. SEM picture of a cross-section of a sample (**a**) built with strategy a, (**b**) built with strategy b and (**c**) built with strategy c, microstructure of the last set of layers, inner layers, and the first set of layers.

4.5. Simplified Thermo-Metallurgical Scheme for AISI 4340

The three different build-up strategies produce different temperature cycles and hardness distributions in the deposited layers. Figure 19 illustrates the relationship between the layer temperature and the average hardness. The hardness value is a mean value of the three curves shown in Figure 14, the temperature value is the average value of the maximum temperatures shown in Figure 13. Only the hardness of the deposited layer was considered for the evaluation. The mean deviation for the hardness and temperature is marked on the bar graph. It can be noticed that the build-up strategies significantly influence the hardness of the deposit. The maximum surface temperature achieved by build-up strategy a, b, and c are 140, 240, and 420 °C, respectively. The average hardness is 470, 350, and 260 HV, accordingly. The cooling time to 60 °C for strategy a is 6 min, for b is 10 min, and for c is 15 min.

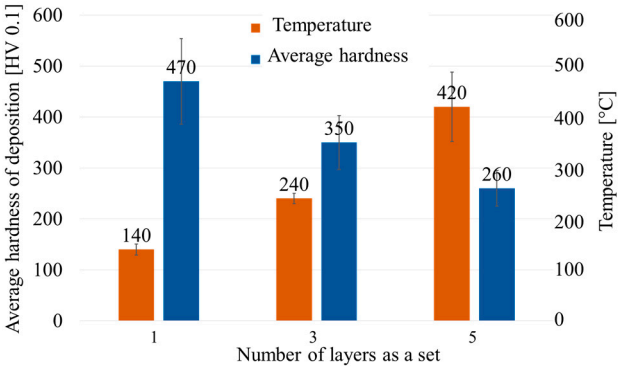

Figure 19. Average hardness of volumes built with different build-up strategies and maximum surface temperature achieved while the deposition process.

5. Tensile Strength for Samples Built-Up by EHLA

As can be seen in Figure 7, samples for the measurement of the tensile strength were produced with build-up strategy c and tested, see Figure 20. Figure 21 shows the measured stress strain curves: Five samples were extracted from the cladded volume, and the tensile results are shown in Figure 21 in different colors. It has no visible yielding stage, and shrinks after uniform plastic deformation, the sample gets fractured when the stress is approximately 900 MPa. It is a typical stress-strain curve of steel treated by low- and medium-temperature tempering after quenching. The highest value of the tensile stress is 1080 MPa and the mean value is 1060 MPa with a scatter of 18 MPa. The average value of yield stress is 880 MPa. The highest and lowest value of elongation is 13.4% and 9.6%, respectively. The tensile strength and the yield strength are higher compared with the annealed AISI 4340 sample (mechanical properties of annealed AISI 4340 alloy steel: Tensile stress: 745 MPa; yield stress: 470 MPa). The elongation of the build-up volume is smaller than that of an annealed one (elongation 22%) due to the existence of brittle phases in the sample. The fracture of specimen (3) appears earlier compared to the other ones; however, the yield strength and tensile strength are similar to the others. The reason for an earlier fracture may be defects in the volume, such as pores or bonding defects.

The fracture surfaces were examined using SEM to understand the fracture mechanism, the image of fracture surface is shown in Figure 22. The fracture mechanism of the deposited specimen appears to be microvoid coalescence which is characterized by numerous dimples, suggesting some degree of brittle failure.

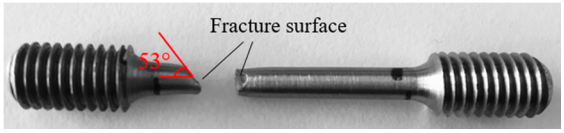

Figure 20. Tensile test sample out of AISI 4340 after testing.

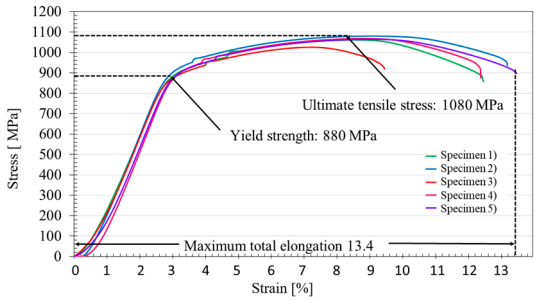

Figure 21. Stress-strain curve for five tested volumes built up with EHLA.

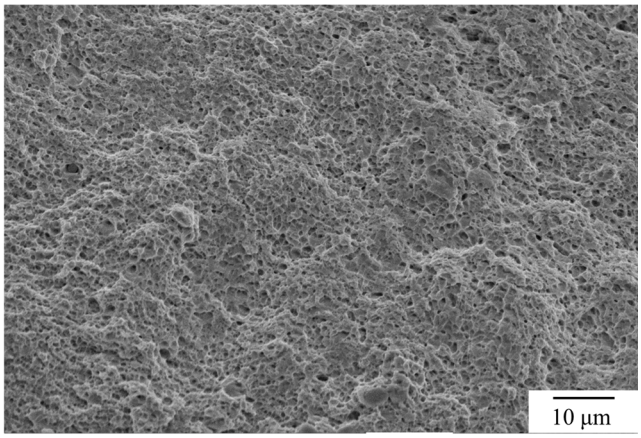

Figure 22. SEM picture of fracture surface of AISI 4340 volumes built up with EHLA.

6. Conclusions

In this investigation, extreme high-speed laser material deposition was used to deposit volumes out of AISI 4340. Not only did we examine the deposition quality by checking the cracks, porosity and bonding quality, but we also studied three different build-up strategies and their influence on the microstructure and hardness, and tested the tensile properties of samples manufactured by EHLA. The main conclusions are as follows:

- EHLA process was utilized to produce deposits out of the AISI 4340 material onto an E355 substrate. The quality examination by optical microscope showed that the deposited layers were crack free, had a porosity level between 0.15% and 3.45%, and sound metallurgical bonding. The HAZ for a single layer is approximately 50 μm.
- The microstructure analysis indicates that a high cooling rate and high temperature gradient lead to the formation of martensite. Increasing the number of deposited layers in each set leads to a coarser microstructure. Knowledge of how different build-up strategies influence temperature evolution and microstructure can be used to control the hardness of the build-up volume in order to meet the requirements of a specific application.
- The hardness measurement shows that hardness is reduced when the number of layers in a set increases between each cooling period. The build-up strategy with cooling time after each layer produces the highest hardness, having a value between 450 and 550 HV 0.1, while the build-up of five layers as a set produces a hardness range of 250 to 350 HV 0.1. The thickness of the heat affected zone is approximately 150 μm for build-up strategy a, 200 μm for build-up strategy b, and 400 μm for build-up strategy c.
- Tensile specimens of build-up volumes show that the yield strength and tensile strength of AISI 4340 samples manufactured by EHLA present superior properties than the forged material. This research gives a simplified thermo-metallurgical scheme for applying the EHLA process to deposit AISI 4340 volumes.
- EHLA process is sufficient to deposit AISI 4340 material onto an E355 substrate with good metallurgical quality. Build-up strategy c with smallest porosity and highest productivity provides a potential way for the build-up of AISI 4340 material.

Author Contributions: Conceptualization, G.G.P.B. and T.L.; methodology, T.S.; validation, G.G.P.B., T.L. and A.G.; formal analysis, A.G.; investigation, T.L.; resources, R.P.; data curation, G.G.P.B.; writing—original draft preparation, T.L.; writing—review and editing, A.G.; supervision, J.H.S., R.P. and L.Z.; project administration, L.Z.; funding acquisition, L.Z.

Funding: This research was funded by Fundamental Research Funds for the Central Universities, grant number 2019JBZ106 and the APC was funded by Fraunhofer-Institut für Lasertechnik ILT.

Conflicts of Interest: The authors declare no conflict of interest. The funders had no role in the design of the study; in the collection, analyses, or interpretation of data; in the writing of the manuscript, or in the decision to publish the results.

References

1. Torres, M.A.S.; Voorwald, H.J.C. An evaluation of shot peening, residual stress and stress relaxation on the fatigue life of AISI 4340 steel. *Int. J. Fatigue* **2002**, *24*, 877–886. [CrossRef]
2. Pape, J.A.; Neu, R.W. A comparative study of the fretting fatigue behavior of 4340 steel and PH 13-8 Mo stainless steel. *Int. J. Fatigue* **2007**, *29*, 2219–2229. [CrossRef]
3. Lee, W.-S.; Su, T.T. Mechanical properties and microstructural features of AISI 4340 high-strength alloy steel under quenched and tempered conditions. *J. Mater. Process. Technol.* **1999**, *87*, 198–206. [CrossRef]
4. Maiti, S.K.; Kishore, G.K.; Mourad, A.H.-I. Bilinear CTOD/CTOA scheme for characterisation of large range mode I and mixed mode stable crack growth through AISI 4340 steel. *Nucl. Eng. Des.* **2008**, *238*, 3175–3185. [CrossRef]
5. Voorwald, H.J.C.; Padilha, R.; Costa, M.Y.P.; Pigatin, W.L.; Cioffi, M.O.H. Effect of electroless nickel interlayer on the fatigue strength of chromium electroplated AISI 4340 steel. *Int. J. Fatigue* **2007**, *29*, 695–704. [CrossRef]
6. Bonora, R.G.; Voorwald, H.J.C.; Cioffi, M.O.H.; Junior, G.S.; Santos, L.F.V. Fatigue in AISI 4340 steel thermal spray coating by HVOF for aeronautic application. *Procedia Eng.* **2010**, *2*, 1617–1623. [CrossRef]
7. Wu, Z.; Huang, C.; Liu, F.; Xia, C.; Ke, L. Microstructure and mechanical properties of 34crnimo6 steel repaired by friction stir processing. *Materials* **2019**, *12*, 279. [CrossRef] [PubMed]
8. Nowotny, S.; Scharek, S.; Beyer, E.; Richter, K.-H. Laser beam build-up welding: Precision in repair, surface cladding, and direct 3D metal deposition. *J. Therm. Spray Technol.* **2007**, *16*, 344–348. [CrossRef]
9. Sexton, L.; Lavin, S.; Byrne, G.; Kennedy, A. Laser cladding of aerospace materials. *J. Mater. Process. Technol.* **2002**, *122*, 63–68. [CrossRef]
10. Paydas, H.; Mertens, A.; Carrus, R.; Lecomte-Beckers, J.; Tchuindjang, J.T. Laser cladding as repair technology for Ti–6Al–4V alloy: Influence of building strategy on microstructure and hardness. *Mater. Des.* **2015**, *85*, 497–510. [CrossRef]
11. Sun, S.D.; Liu, Q.; Brandt, M.; Luzin, V.; Cottam, R.; Janardhana, M.; Clark, G. Effect of laser clad repair on the fatigue behaviour of ultra-high strength AISI 4340 steel. *Mater. Sci. Eng. A* **2014**, *606*, 46–57. [CrossRef]
12. Chew, Y.; Pang, J.H.L.; Bi, G.; Song, B. Effects of laser cladding on fatigue performance of AISI 4340 steel in the as-clad and machine treated conditions. *J. Mater. Process. Technol.* **2017**, *243*, 246–257. [CrossRef]
13. Sun, G.; Zhou, R.; Lu, J.; Mazumder, J. Evaluation of defect density, microstructure, residual stress, elastic modulus, hardness and strength of laser-deposited AISI 4340 steel. *Acta Mater.* **2015**, *84*, 172–189. [CrossRef]
14. Digital Photonic Production along the Lines of Industry 4.0. Available online: https://www.spiedigitallibrary.org/conference-proceedings-of-spie/10519/1051907/Digital-photonic-production-along-the-lines-of-industry-40/10.1117/12.2292316.short (accessed on 20 November 2019).
15. Schopphoven, T.; Gasser, A.; Backes, G. EHLA: Extreme High-Speed Laser Material Deposition: Economical and effective protection against corrosion and wear. *Laser Tech. J.* **2017**, *14*, 26–29. [CrossRef]
16. Matthiesen, G. Additive manufacturing processes in fluid power–properties and opportunities demonstrated at a flow-optimized fitting. In Proceedings of the 2018 International Conference on Hydraulics and Pneumatics – HERVEX, Băile Govora, Romania, 7–9 November 2018; pp. 12–23.
17. Liu, Q.; Janardhana, M.; Hinton, B.; Brandt, M.; Sharp, K. Laser cladding as a potential repair technology for damaged aircraft components. *Int. J. Struct. Integr.* **2011**, *2*, 314–331. [CrossRef]
18. *ISO 6892-1: 2016: Metallic Materials—Tensile Testing—Part 1: Method of Test at Room Temperature*; ISO: Geneva, Switzerland, 2016.
19. *ISO 6892-1: 2009: Metallic Materials—Tensile Testing—Part 1: Method of Test at Room Temperature*; ISO: Geneva, Switzerland, 2009.
20. Dodds, S.; Jones, A.H.; Cater, S. Tribological enhancement of AISI 420 martensitic stainless steel through friction-stir processing. *Wear* **2013**, *302*, 863–877. [CrossRef]
21. Materkowski, J.P.; Krauss, G. Tempered martensite embrittlement in SAE 4340 steel. *Metall. Trans. A* **1979**, *10*, 643–1651. [CrossRef]

22. McDaniels, R.L.; White, S.A.; Liaw, K.; Chen, L.; McCay, M.H.; Liaw, P.K. Effects of a laser surface processing induced heat-affected zone on the fatigue behavior of AISI 4340 steel. *Mater. Sci. Eng. A* **2008**, *485*, 500–507. [CrossRef]
23. Costa, L.; Vilar, R.; Reti, T.; Deus, A.M. Rapid tooling by laser powder deposition: Process simulation using finite element analysis. *Acta Mater.* **2005**, *53*, 3987–3999. [CrossRef]
24. Capello, E.; Colombo, D.; Previtali, B. Repairing of sintered tools using laser cladding by wire. *J. Mater. Process. Technol.* **2005**, *164*, 990–1000. [CrossRef]